

## Article

# Nonradiative Energy Transfer in $\text{Bi}_2\text{O}_3/\text{Tm}_2\text{O}_3$ Powders under IR Excitation at Liquid Nitrogen Temperature

Dmitry A. Artamonov <sup>1</sup>, Anna V. Tsibulnikova <sup>1,\*</sup>, Vasily A. Slezkin <sup>1,2</sup>, Alexey S. Kozhevnikov <sup>1</sup>, Ilia G. Samusev <sup>1</sup>, Ivan I. Lyatun <sup>1</sup> and Valery V. Bryukhanov <sup>1</sup>

<sup>1</sup> REC Fundamental and Applied Photonics. Nanophotonics, Immanuel Kant Baltic Federal University, 14 Nevskogo Street, Kaliningrad 236016, Russia

<sup>2</sup> Kaliningrad Technical State University, 1 Sovetsky Ave, Kaliningrad 236000, Russia

\* Correspondence: memorgold@mail.ru

**Abstract:** The presented work shows the study of energy transitions in the NIR and visible regions in the system of  $\text{Bi}_2\text{O}_3$  and  $\text{Tm}_2\text{O}_3$  powders. Mechanisms of upconversion luminescence and NIR luminescence between two  $\text{Bi}^{3+}$  and  $\text{Tm}^{3+}$  ions at  $T = 80$  K accompanied with nonradiative energy transfer through the vibrational levels were investigated under IR photoexcitation. The absorption bands of the samples on the reflection spectra were examined in the visible region. The values of the emission cross-section parameters were calculated for the  $\text{Bi}_2\text{O}_3/\text{Tm}_2\text{O}_3$  complexes.

**Keywords:** energy transfer; upconversion luminescence; low temperatures; reflectance; level splitting

## 1. Introduction



**Citation:** Artamonov, D.A.; Tsibulnikova, A.V.; Slezkin, V.A.; Kozhevnikov, A.S.; Samusev, I.G.; Lyatun, I.I.; Bryukhanov, V.V. Nonradiative Energy Transfer in  $\text{Bi}_2\text{O}_3/\text{Tm}_2\text{O}_3$  Powders under IR Excitation at Liquid Nitrogen Temperature. *Crystals* **2023**, *13*, 534. <https://doi.org/10.3390/crust13030534>

Academic Editors: Tzi-yi Wu and Ali Belarouci

Received: 27 February 2023

Revised: 17 March 2023

Accepted: 18 March 2023

Published: 20 March 2023



**Copyright:** © 2023 by the authors. Licensee MDPI, Basel, Switzerland. This article is an open access article distributed under the terms and conditions of the Creative Commons Attribution (CC BY) license (<https://creativecommons.org/licenses/by/4.0/>).

In recent years, there has been a great interest in the conversion of IR radiation to shorter wavelengths using materials doped with a rare-earth element (REE), such as  $\text{Tm}^{3+}$ ,  $\text{Er}^{3+}$ ,  $\text{Ho}^{3+}$  [1,2]. Solid-state compact matrices based on REEs have become the subject of intensive spectroscopic studies due to their potential application as laser media for the visible range with upconversion (UC) emission [3–5]. High quantum efficiency solves the problem of the limited efficiency of silicon solar cells due to dopanding the different combinations of rare earth ions such as  $\text{Tb}^{3+}$ - $\text{Yb}^{3+}$  and  $\text{Tm}^{3+}$ - $\text{Yb}^{3+}$ . The activated ions convert the high-energy part of the solar spectrum to the NIR wavelength region [6,7]. The  $\text{Tm}^{3+}$  ion has rich spectral energy levels in the range from the UV to the IR region. In addition,  $\text{Tm}^{3+}$  ions play a key role as an active dopant in doping in various solid media to produce laser radiation via an upconversion activation mechanism [8–10].

At the same time, the presence of wide energy levels in the bismuth ion of different valency is well known, which cause the possibility of photoluminescence generation and inter-level energy transfer in the presence of other closely located ions [11–14]. NIR luminescence has been observed at 1210 nm, 1173 nm and 1300 nm in quartz glasses doped with bismuth ions when the glass was irradiated by wavelengths of 405 nm and 808 nm, respectively [15,16]. It should be noted that the structure of glass significantly influences the hardness, density, refractive index and optical properties of glass, affecting the position of emission maxima, intensity and half-width of the maximum emission of Bi ions [17–19]. The low-temperature conditions are extremely important to observe energy transitions with single-band and narrow emission peaks in systems consisting of two different RE ions [20–22]. Thus, in conditions of low temperatures of liquid nitrogen due to spectral splitting of energy levels, spectral shifts in photoluminescence spectra in the NIR region are also possible [23]. The present work is a continuation of our previous work on the study of photo processes involving REE ions [20,24,25].

Since changes in the luminescence spectra of REE can be observed at low temperatures and since energy-transfer processes through energy levels are possible, due to the overlap of the  $\text{Bi}^{3+}$  and  $\text{Tm}^{3+}$  spectral bands in the visible region, a mixture of  $\text{Bi}_2\text{O}_3/\text{Tm}_2\text{O}_3$  oxides

is an interesting subject as an optical element for luminescence generation in the visible-IR ranges. Therefore, the purpose of this work was to establish the phase composition of the oxide mixture and to determine the necessary atomic ratios at which the generation of luminescent properties in the  $\text{Bi}_2\text{O}_3/\text{Tm}_2\text{O}_3$  system is possible. In addition, the key photophysical task of this study was to establish the spectral features of the upconversion luminescence of the oxides system and the ways of photoexcitation energy degradation at low temperatures.

## 2. Materials and Methods

### 2.1. Preparation of $\text{Bi}_2\text{O}_3$ with $\text{Tm}_2\text{O}_3$ Powders

Bismuth oxide was prepared by dissolving metallic bismuth (purity of 99.999%) mass of  $m = 2 \text{ g}$  in the nitric acid with following preparation of bismuth oxalate and sintering in a muffle oven at a temperature of  $T = 750 \text{ }^\circ\text{C}$  for 2 h. A detailed description of the synthesis technique was presented in [24,26]. The obtained powder was light-yellow color. Then the obtained  $\text{Bi}_2\text{O}_3$  was mixed with  $\text{Tm}_2\text{O}_3$  (purchased from Sigma-Aldrich, St. Louis, MO, USA, purity of 99.999%). The powders were grinded in a mortar for 60 min. Then powder mixture was pressed into a pellet and annealed at a temperature of  $750 \text{ }^\circ\text{C}$  for 2 h. The atomic concentration of  $\text{Tm}^{3+}$  changed in the range of (2.3–28) at.%.

### 2.2. Experimental Measurements

Luminescence experiments were performed by means of a Fluorolog-3 optical system (Horiba and Jobin Yvon Technology, Horiba Scientific, Palaiseau, France) equipped with an FL-1073 detector operating in the UV-VIS radiation bands. The IR laser (model LSR-PS-II) (China Ningbo Fingco Optoelectronic Co., Ltd., Ningbo, China) with continuously adjustable energy (0.1–1.0 W) and a wavelength of 980 nm was used as an excitation source. A cooled solid-state IR detector (Horiba Scientific, Longjumeau Cedex, France) (model 1427C) with a PS/TC-1 controller was used to measure luminescence in the infrared region.

The XRD pattern of the powders was recorded with using Dron-3 diffractometer Radikon LLC X-ray (Burevestnik, Ufa, Russia).

The morphological features of the oxides were studied by scanning electron microscopy on the Zeiss Cross Beam-540 FIBSEM (Zeiss, Oberkochen, Germany). The SEM/EDX analysis of the powders was examined by means of JEOL JSM-6390LV scanning electron microscope (Akishima, Tokyo, Japan) equipped with an Oxford instrument Inca X-Act SSD energy dispersive X-ray spectrometer. Secondary electron images and EDX data of the powders were obtained at 20 kV accelerating voltage.

The reflection spectra were measured on a spectrophotometer (Shimadzu, Kyoto, Japan) with an integrating sphere application in the range of 200–800 nm.

## 3. Results and Discussion

In the first series of the experiment, X-ray diffraction analysis of the studied powders and their morphological features were carried out. Figure 1 shows the XRD pattern of the  $\text{Tm}_2\text{O}_3$ ,  $\text{Bi}_2\text{O}_3$ ,  $\text{Bi}_2\text{O}_3/\text{Tm}_2\text{O}_3$  (22 at.%) oxides.

According to the X-ray analysis, the  $\text{Tm}_2\text{O}_3$  has a cubic body centered lattice with the type of symmetry Ia3 (card No.631) with the following parameters of the unit cell: The length of the cube edge— $a = 10.45 \text{ \AA}$ , the number of formula units included in the unit cell— $Z = 16$  (32 atoms of Tm and 48 atoms of O). Bismuth oxide has a monoclinic lattice with the space group of a P 21/c (card No. 2-498). The unit cell parameters are:  $a = 5.83 \text{ \AA}$ ,  $b = 8.14 \text{ \AA}$ ,  $c = 7.48 \text{ \AA}$ ,  $\alpha = 90^\circ$ ,  $\beta = 67.7^\circ$ ,  $\gamma = 90^\circ$ . A comparison was made with the PDWin base library for the most intense XRD pattern peaks.

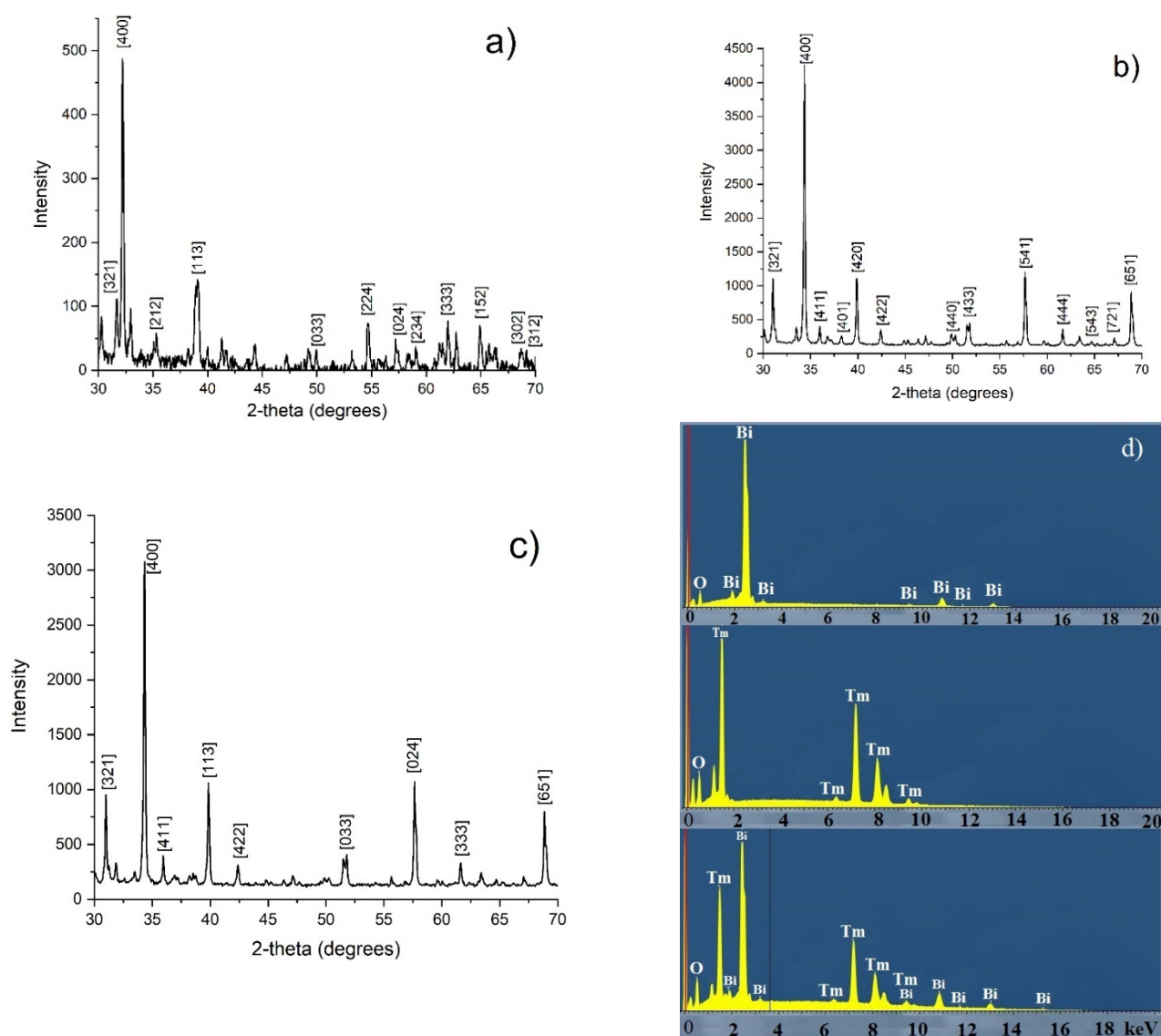


**Figure 1.** XRD patterns of the oxides  $\text{Bi}_2\text{O}_3$ —(a);  $\text{Tm}_2\text{O}_3$ —(b);  $\text{Bi}_2\text{O}_3/\text{Tm}_2\text{O}_3$  (28 at.%)—(c); EDX analysis with atomic concentrations—(d).

The interplanar distances (d) corresponding to  $\text{Bi}_2\text{O}_3$  and  $\text{Tm}_2\text{O}_3$  in the mixture are presented in Table 1.

As can be seen from Figure 1c, on the diffraction pattern corresponding to the mixture of the oxides and Table 1 containing the peaks, in the structure of the powder, peaks corresponding to the two main phases were observed: cubic lattice ( $\text{Tm}_2\text{O}_3$ ) and monoclinic lattice ( $\text{Bi}_2\text{O}_3$ ). However, in the spectrum presented in Figure 1c, there were no intense reflexes [224] and [152] corresponding to the monoclinic  $\text{Bi}_2\text{O}_3$  phase. In this regard, it can be concluded that as a result of sintering, the transformation of the crystal lattice of bismuth oxide occurs. Thus, during the annealing process at  $T = 750\text{ }^\circ\text{C}$ , as a result of surface diffusion in the mixture, a new phase is formed in the surface layer of the mixture ( $\text{Bi}_2\text{O}_3/\text{Tm}_2\text{O}_3$ ), while in the depth of the composition of the mixture, the main phase composition remains.

**Table 1.** The most intense XRD pattern reflections characteristic of the  $\text{Bi}_2\text{O}_3$  and  $\text{Tm}_2\text{O}_3$  content in the  $\text{Bi}_2\text{O}_3/\text{Tm}_2\text{O}_3$  (28 at.-%).

| $\text{Bi}_2\text{O}_3$ |       | $\text{Tm}_2\text{O}_3$ |       |
|-------------------------|-------|-------------------------|-------|
| 2θ (Degree)             | d (Å) | 2θ (Degree)             | d (Å) |
| 31.000                  | 2.882 | 31.850                  | 2.807 |
| 35.300                  | 2.540 | 33.200                  | 2.696 |
| 45.250                  | 2.002 | 33.500                  | 2.673 |
| 45.950                  | 1.973 | 34.350                  | 2.609 |
| 46.350                  | 1.957 | 38.250                  | 2.351 |
| 53.650                  | 1.707 | 57.650                  | 1.598 |
| 54.250                  | 1.689 | 59.600                  | 1.550 |
| 54.700                  | 1.677 | 61.650                  | 1.503 |
| 55.650                  | 1.650 | 63.400                  | 1.466 |
| 62.831                  | 1.478 | 64.700                  | 1.440 |
| 65.800                  | 1.418 | 67.106                  | 1.619 |

To determine the elemental composition of the synthesized samples, the studies were supplemented with the EDX spectral analysis. The spectral elemental composition of the mixture was performed in the  $10 \mu\text{m}^2$  area of the investigated powder with following averaging of the spectrum. Thus, the elemental composition for samples  $\text{Bi}_2\text{O}_3$ ,  $\text{Tm}_2\text{O}_3$  and  $\text{Bi}_2\text{O}_3/\text{Tm}_2\text{O}_3$  in atomic percentages is shown in Figure 1d. Therefore, Figure 1d demonstrates that the synthesis method presented in this paper is a suitable method to obtain sufficiently homogeneous oxides without foreign impurities in the specified temperature range. The EDX-analysis for different atomic concentration of the thulium and bismuth ions presented in the supplementary materials.

The presence of an additional phase of thulium oxide in the microstructure of the mixture  $\text{Bi}_2\text{O}_3/\text{Tm}_2\text{O}_3$  affects the X-ray diffraction analysis. Thus, on the diffraction pattern corresponding to the mixture of oxides (Figure 1c), the partial or complete quenching of individual peaks characteristic of the phase composition of a single component is observed.

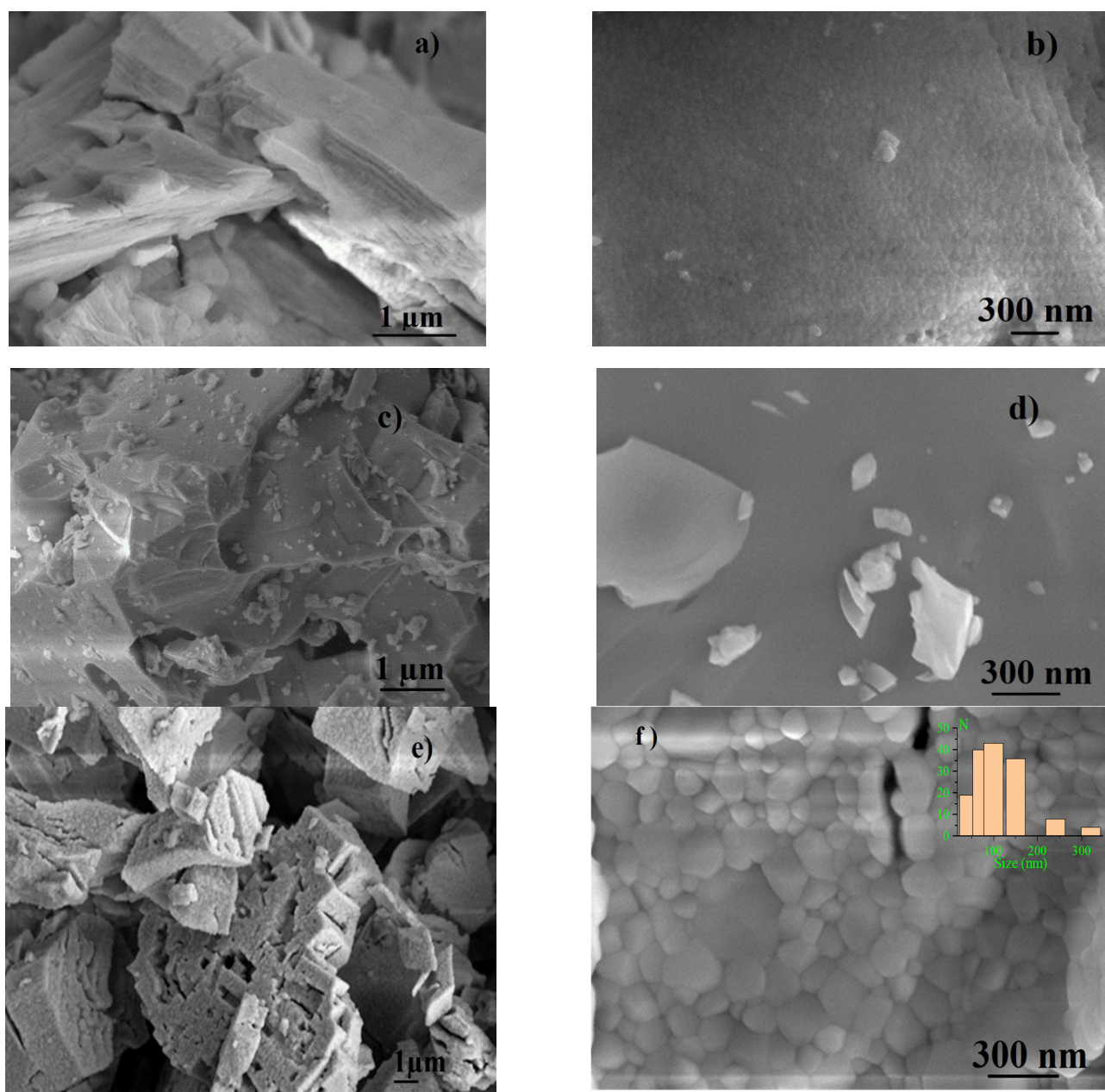
Next, it was of interest to consider the morphological features of the studied oxides. Figure 2 shows the results of SEM microscopy of the powders.

Figure 2a shows that the surface structure of  $\text{Tm}_2\text{O}_3$  is homogeneous without the periodic clusters formation. In the cross-section, a plate-like structure with a height of  $\approx 0.1 \mu\text{m}$  is observed. The structure of the formations is dense with large layered formations. In Figure 2b, they are a solid, to the cells' similar structure.

Figure 2c shows that the surface of  $\text{Bi}_2\text{O}_3$  consists of clusters with an average size of  $1 \mu\text{m}$ . The surface of  $\text{Bi}_2\text{O}_3$  is smooth without roughness. When looking at the surface on the scale of  $200 \text{ nm}$ , there are no cellular structures as it was observed for  $\text{Tm}_2\text{O}_3$  (Figure 2b). Periodicity in the formation of the structure is also not observed. There are irregularities with the formation of internal tunnels with an average diameter of  $3 \mu\text{m}$ .

Figure 2e,f shows that the  $\text{Bi}_2\text{O}_3/\text{Tm}_2\text{O}_3$  complex has a granular surface structure.

Thus, the inset of Figure 2f shows a diagram of the quantitative distribution of granules by size. The diagram was constructed based on a detailed analysis of the SEM image from Figure 2f. Thus, the linear dimensions of crystal structures with a mathematical ratio of the image scale of Figure 2f ( $300 \text{ nm}$ ) were estimated on an area of  $3.96 \mu\text{m}^2$ . Therefore, the size of granules in a mixture of  $\text{Bi}_2\text{O}_3/\text{Tm}_2\text{O}_3$  with the atomic concentration of thulium ions of 28 at.% varies in the range of  $50\text{--}320 \text{ nm}$ . The average linear size was calculated by using quantitative-numerical analysis, considering the total number of granules (150). Thus, the average size was approximately  $100 \text{ nm}$ .



**Figure 2.** SEM images of the powders at different scales: (a,b)— $\text{Tm}_2\text{O}_3$ ; (c,d)— $\text{Bi}_2\text{O}_3$ ; (e,f)— $\text{Bi}_2\text{O}_3/\text{Tm}_2\text{O}_3$ . Insert—size distribution of the crystallites.

The structure presents a columnar formation with a rough surface height of  $12 \mu\text{m}$ . The shape of the grains is rounded; the density of the grains is high without appreciable porosity. The arrangement is chaotic over the entire surface of the sample. The formation of cellular structures due to the presence of bismuth oxide in the mixture is also characteristic here.

Then, the luminescence studies of the  $\text{Bi}_2\text{O}_3/\text{Tm}_2\text{O}_3$  mixture in the visible and infrared regions at liquid nitrogen temperature were carried out under conditions of changing the atomic concentration of  $\text{Tm}^{3+}$  in the mixture.

Let us consider how the intensity of  $\text{Bi}^{3+}$  luminescence changes with a change in the concentration of  $\text{Tm}^{3+}$  in the NIR region. As a result of the  $\text{Tm}^{3+}$  presence, an increase in the IR luminescence of  $\text{Bi}^{3+}$  was observed. It is important to point out a linear type of the concentration dependence of intensity (inset Figure 3a). Therefore, at the lowest concentration of  $\text{Tm}^{3+}$  (2.3 at.%), the maximum value of the NIR luminescence intensity at the  $1240 \text{ nm}$  wavelength was observed and amounted up to  $I = 2000 \mu\text{V}$ . At the same

time, the formation of a new spectral maximum at a wavelength of 1280 nm was found. It is important to note that when a single thulium oxide powder was excited under photoexcitation with a wavelength of 980 nm at 80 K, no luminescence signal was observed in the  $\text{Tm}_2\text{O}_3$  powder. Hence, the obtained spectral maxima in the NIR region are due to  ${}^3\text{P}_1 \rightarrow {}^3\text{P}_0$  transitions for  $\text{Bi}^{3+}$  atoms. The appearance of the maximum at 1280 nm apparently could be due to the influence of the  $\text{Tm}_2\text{O}_3$  crystal field surrounding the  $\text{Bi}^{3+}$  atoms. As a result of the influence of the additional field at low nitrogen temperatures, the excited  ${}^3\text{P}_1$  level splits into Stark sublevels. The magnitude of the splitting of the main electron term ( ${}^3\text{P}_1$ ) can reach up to  $1000 \text{ cm}^{-1}$  [27], and since the emission wavelength lags behind the main maximum by 40 nm, consequently the value of the Stark splitting is  $\Delta E \approx 200 \text{ cm}^{-1}$ . As a result of the activation of ultrafast processes ( $>10^{-12} \text{ s}$ ) of absorbed energy degradation (wavelength 980 nm) between vibrational sublevels (internal conversion) at low temperatures, emission transitions of microsecond duration can be observed [28,29]. The mechanisms of energy transfer and ways of energy degradation in the complex by energy levels are discussed below.

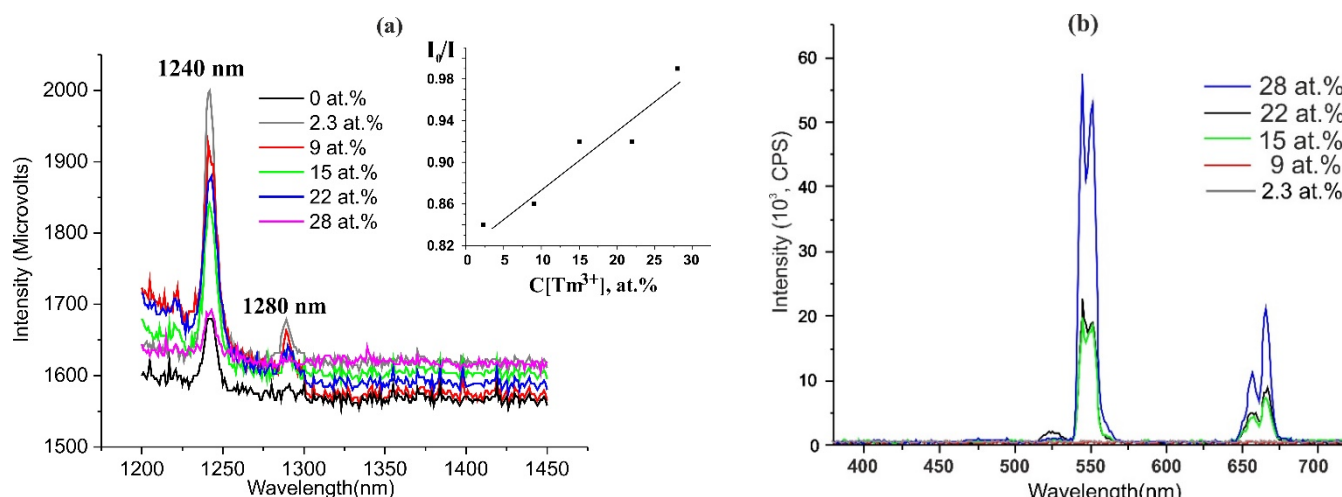


**Figure 3.** Luminescence spectra in the infrared region (a) and upconversion luminescence spectra in the visible region (b) of  $\text{Bi}_2\text{O}_3/\text{Tm}_2\text{O}_3$  powders with different concentrations of  $\text{Tm}^{3+}$  atoms (2.3–28). The excitation wavelength  $\lambda_{\text{ex}} = 980 \text{ nm}$ ,  $T = 80 \text{ K}$ .

Let us consider the processes of luminescence of powders in the visible region under photoexcitation with a wavelength of 980 nm. In the region of green wavelengths and red wavelengths, emission maxima due to the upconversion mechanism of luminescence were observed. The lifetimes of the upconversion luminescence are 172 ns and 670 ns at 545 nm and 665 nm, respectively. The kinetic curves are shown in Figure 4. With an increase in the atomic concentration of thulium ions, an increase in the intensity of upconversion luminescence at wavelengths in the region of 550 and 670 nm has occurred (Figure 3b). The highest UCL intensity corresponds to the maximum of  $\text{Tm}^{3+}$  concentration (28 at.%).

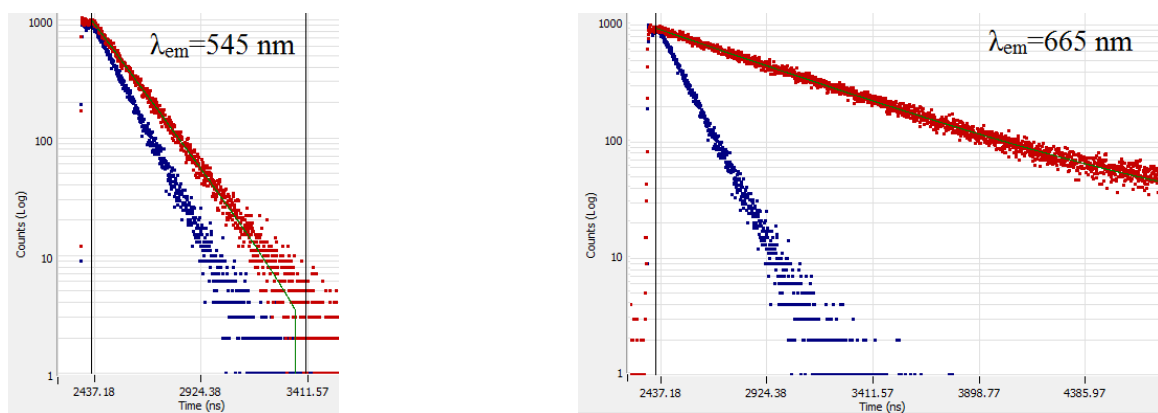


**Figure 4.** Kinetic decay curves (red curves) of UCL recorded at 545 nm and 665 nm under excitation with wavelengths of 980 nm (concentration of  $\text{Tm}^{3+}$  was of 28 at.%) at  $T = 80 \text{ K}$ . Blue curves—excitation source pulse.

The energy diagram of  $\text{Tm}^{3+}$  and  $\text{Bi}^{3+}$  ions, taking into account the theoretical data [30,31] and experimentally observed transitions in the visible and infrared regions at nitrogen temperature, is shown in Figure 5.

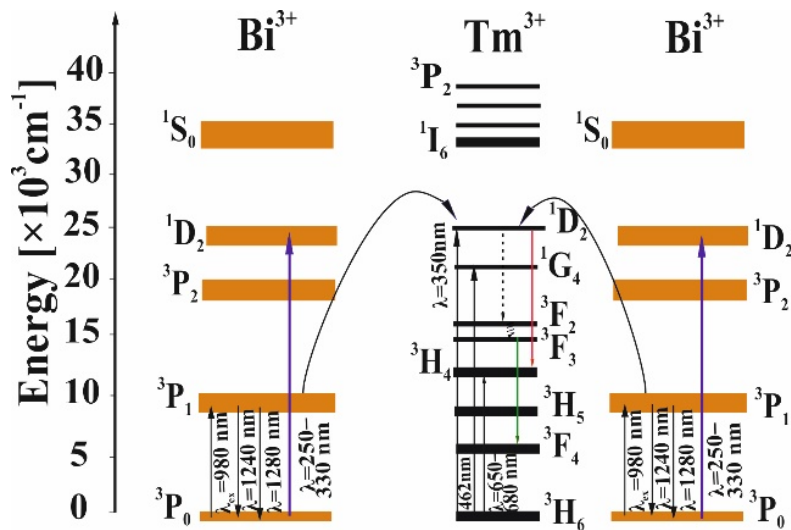


**Figure 5.** Energy diagram of  $\text{Tm}^{3+}$  and  $\text{Bi}^{3+}$  ions with experimentally observed transitions in the visible and infrared regions at  $T = 80 \text{ K}$ .

Thus, the process of the appearance of UCL in the visible region is due to the simultaneous excitation of two  $\text{Bi}^{3+}$  ions with a wavelength of 980 nm, accompanied by a transition between levels  $^3\text{P}_0 \rightarrow ^3\text{P}_1$ . The absorbed energy is deactivated in the form of luminescence at a wavelength of 1240 nm and 1280 nm from two vibrational sublevels of one electronic energy level ( $^3\text{P}_1$ ). At the same time, the total energy of two excited  $\text{Bi}^{3+}$  ions after absorption of a quantum with a wavelength of 980 nm accumulates at a higher level of  $^1\text{D}_2$ , corresponding to the mechanism of cooperative sensitization [16,27,32] accompanied by deactivation of UCL in the red region ( $^1\text{D}_2 \rightarrow ^3\text{H}_4$ ). Further, by ultrafast intercombination conversion  $^1\text{D}_2 \rightarrow ^3\text{F}_2$  and deactivation of  $^3\text{F}_2 \rightarrow ^3\text{F}_3$ , a transition of  $^3\text{F}_3 \rightarrow ^3\text{F}_4$  is observed in the green area. Therefore, based on the presented data it can be concluded that in the system ( $\text{Bi}^{3+}$ - $\text{Bi}^{3+}$ )- $\text{Tm}^{3+}$  it is possible to observe the nonradiative energy transfer with the UCL and NIR emission activation. This energy transfer could be considered just at low temperature to produce the mechanism of acceleration of energy degradation through the vibration levels.

Further, it was of interest to determine the cross-section of the UCL emission at the observed wavelengths using the following equation [29]:

$$\sigma_{\text{em}} = \frac{\lambda_0^2}{4\pi n^2 c \tau \Delta\lambda} \left( \frac{\ln 2}{\pi} \right)^{0.5} \quad (1)$$

where  $\lambda_0$  is the emission wavelength,  $n$  is the refractive index,  $\tau$  is the UCL lifetime,  $c$  is the speed of light and  $\Delta\lambda$  is the half-width of the UCL spectrum.

Substituting the following values into the equation:  $n = 2$ ;  $\Delta\lambda \approx 10$  nm;  $\tau = 172$  ns and  $\tau = 664$  ns for  $\lambda_0 = 550$  and  $\lambda_0 = 665$  nm, respectively, it can be calculated:

$$\sigma_{\text{em}} = 29.3 \times 10^{-17} \text{ cm}^2 \text{ (for } \lambda_0 = 550 \text{ nm)} \text{ and } \sigma_{\text{em}} = 62.7 \times 10^{-17} \text{ cm}^2 \text{ (for } \lambda_0 = 660 \text{ nm).}$$

The multiplication of  $\sigma_{\text{em}}$  and  $\tau$  was also calculated:  $\sigma_{\text{em}}\tau = 0.5 \times 10^{-22} \text{ cm}^2 \text{ s}$  (for  $\lambda_0 = 550$  nm) and  $4.1 \times 10^{-22} \text{ cm}^2 \text{ s}$  (for  $\lambda_0 = 660$  nm).

These obtained values are well-correlated with the theoretical data [33] and indicate that the resulting powder of  $\text{Bi}_2\text{O}_3/\text{Tm}_2\text{O}_3$  with a cell-like structure (Figure 2e,f) can generate an intense luminescence in the visible region under IR excitation with an acceptable value of the emission cross-section of the crystal structure.

Due to the presence of UCL luminescence in the visible region of the spectrum, it is important to consider the reflectance spectra of the powders in the UCL region. The reflection spectra at liquid nitrogen temperatures are presented in Figure 6.

In the reflection spectra, the absorption bands at wavelengths of 350,360 nm correspond to the transition  ${}^3\text{H}_6 \rightarrow {}^1\text{D}_2$  in  $\text{Tm}^{3+}$ ; bands at 463, 475 nm correspond to  ${}^3\text{H}_6 \rightarrow {}^1\text{G}_4$ ; and bands at wavelengths of 650–680 nm correspond to the  ${}^3\text{H}_6 \rightarrow {}^3\text{H}_4$  transition. The wide absorption band for  $\text{Bi}^{3+}$  at 400 nm is associated with the  ${}^1\text{S}_0 \rightarrow {}^3\text{P}_1$  transition.

A few brief notes can be made on the spectral features recorded at low temperatures. Thus, when considering a reflectance spectrum obtained for  $\text{Bi}_2\text{O}_3$  powder without  $\text{Tm}_2\text{O}_3$  at  $T = 80$  K (Figure 6a), there are two minima in the ultraviolet region: at 254 nm and 306 nm (with a value of  $R \approx 47\%$ ) and a peak at 400 nm. In all powders, the wide absorption peak at 400 nm corresponding to  $\text{Bi}_2\text{O}_3$  is presented. For instance, at  $T = 293$  K no peaks in ultraviolet were observed (Figure 6b). In addition, at  $T = 80$  K, a minimum in the reflection function in the green region (566 nm) for  $\text{Bi}_2\text{O}_3$  powder has occurred.

The reflection coefficient 22 at.% at 420 nm at  $T = 80$  K increased 3.2 times.

When considering a sample of  $\text{Tm}_2\text{O}_3$  in the absence of  $\text{Bi}_2\text{O}_3$ , the reflection coefficient in the whole considered absorption range at  $T = 80$  K increases 1.5–4 times in comparison with the reflection function recorded at  $T = 293$  K. In addition, the appearance of clearly resolved minima in the UV region (on 286 and 225 nm) for  $\text{Tm}_2\text{O}_3$  oxide (Figure 6a) should be noted.

Figure 6c shows that the reflection coefficient does not change linearly by increasing the  $\text{Tm}^{3+}$  concentration at  $T = 80$  K. At the concentration of 15 at.%, the maximum value of the reflection coefficient at all considered wavelengths is observed. The highest value of the coefficient ( $R = 55\%$ ) corresponds to the wavelength of 665 nm. At  $T = 293$  K, the dynamics of the reflection coefficient changes linearly in all spectral ranges. The other optical constants (refractive index, dielectric permittivity functions and polarization) of the material and the reflection coefficients at room temperature depending on the  $\text{Tm}^{3+}$  concentration are presented in the supplementary materials.

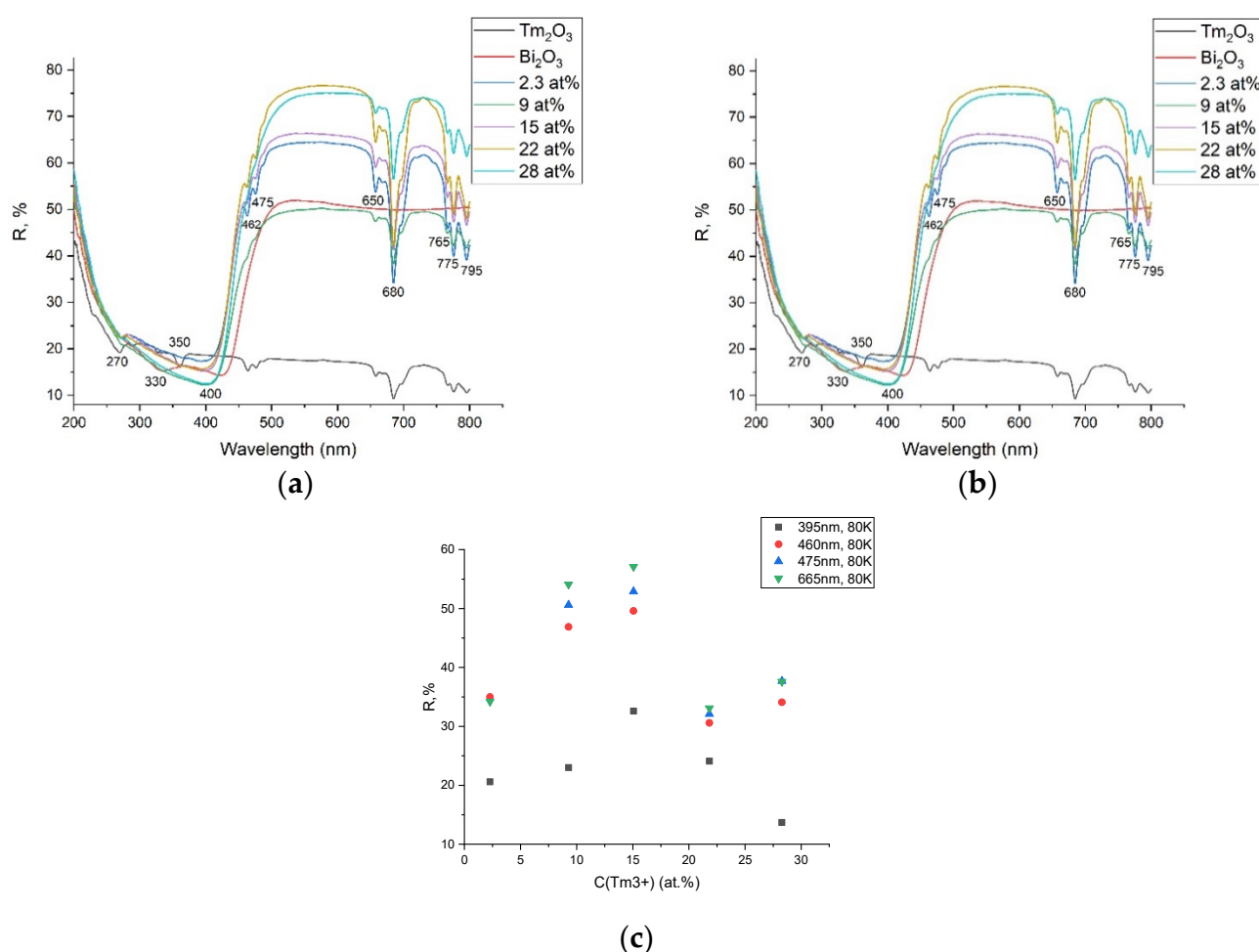


**Figure 6.** Reflection spectra of  $Bi_2O_3/Tm_2O_3$  oxides with different atomic concentrations of  $Tm^{3+}$  in the mixture (2.3–28 at.%) at  $T = 80\text{ K}$  (a), at  $T = 293\text{ K}$  (b) and dynamic of  $R(\%)$  depending on the  $Tm^{3+}$  concentration at  $T = 80\text{ K}$  (c).

#### 4. Conclusions

A two-component material  $Bi_2O_3/Tm_2O_3$  with granule sizes of about 100 nm was synthesized in this work. Based on the X-ray diffraction analysis data, the presence of a cubic phase for thulium oxide and a monoclinic phase for bismuth oxide was established. In addition, the presence of additional peaks on the diffraction pattern for the mixture was due to the transformation of the crystal lattice of bismuth oxide in the presence of thulium oxide in the process of temperature synthesis.

It was shown that the synthesized complex of  $Bi_2O_3/Tm_2O_3$  with a specific surface granular structure is capable of emission in the NIR region and luminescence by the mechanism of upconversion in the red and green regions of the visible spectral range at low temperatures ( $T = 80\text{ K}$ ). It was established that upconversion energy transfer is a result of nonradiative energy transfer in the  $(Bi^{3+}-Bi^{3+})-Tm^{3+}$  system. The upconversion luminescence lifetimes in the visible region of the spectrum were  $\tau = 172\text{ ns}$  and  $\tau = 664\text{ ns}$  for  $\lambda = 550$  and  $\lambda = 665\text{ nm}$ , respectively. The calculated values of the emission cross-section indicate a sufficiently efficient conversion of the IR absorbed energy with a nanosecond deactivation duration.

At the same time, the presence of two-band IR luminescence (1250 nm and 1280 nm) of the  $Bi_2O_3/Tm_2O_3$  complex at liquid nitrogen temperature was established. It was shown that the intensity of IR luminescence from the concentration of thulium ions in the mixture was determined by a linear dependence. NIR luminescence in the region of 1240 and 1280 nm was due to the absorption by  $Bi^{3+}$  ions of a wavelength of 980 nm and energy

deactivation through the  $^3P_1 \rightarrow ^3P_0$  levels. Studies of reflection spectra in the visible region at low temperatures have shown the presence of the spectrum splitting for thulium oxide in the UV region. The concentration dependences of the reflection coefficient at the absorption wavelengths were determined by a nonlinear dependence during spectral measurements at liquid nitrogen temperatures.

**Supplementary Materials:** The following supporting information can be downloaded at: <https://www.mdpi.com/article/10.3390/cryst13030534/s1>, Figure S1: The EXD analysis of the samples with the different atomic concentrations of the thulium and bismuth ions; Figure S2: The dynamic of R(%) depending on the  $Tm^{3+}$  concentration at  $T = 293$  K at absorption wavelength (395, 460, 474, 665 nm); Figure S3: Kinetic decay curves of UCL recorded at 665 nm under excitation with wavelengths of 980 nm (concentration of  $Tm^{3+}$  was of 15 at.% and 22 at.%) at  $T = 80$  K; Figure S4: Refractive index spectrum in visible region for  $Bi_2O_3/Tm_3O_3$  system. Figure S5: Complex dielectric function in visible region for  $Bi_2O_3/Tm_3O_3$  system; Figure S6: Polarization in visible region for  $Bi_2O_3/Tm_3O_3$  system.

**Author Contributions:** D.A.A.—sample preparation, measurements; A.V.T.—conceptualization, original draft preparation; V.A.S.—data analysis; A.S.K.—investigation; I.G.S.—project administration; I.I.L.—investigation, data analysis; V.V.B.—data curation. All authors have read and agreed to the published version of the manuscript.

**Funding:** This research received no external funding. The APC was funded by Immanuel Kant Baltic Federal University.

**Data Availability Statement:** The data presented in this study are available from the corresponding authors upon reasonable request.

**Conflicts of Interest:** Authors declare no conflict of interests.

## References

- Matsuura, D. Red, Green, and Blue Upconversion Luminescence of Trivalent-Rare-Earth Ion-Doped  $Y_2O_3$  Nanocrystals. *Appl. Phys. Lett.* **2002**, *81*, 4526–4528. [[CrossRef](#)]
- Desirena, H.; De La Rosa, E.; Romero, V.H.; Castillo, J.F.; Díaz-Torres, L.A.; Oliva, J.R. Comparative Study of the Spectroscopic Properties of  $Yb_3/Er_3$  Codoped Tellurite Glasses Modified with  $R_2O$  ( $R = Li, Na$  and  $K$ ). *J. Lumin.* **2012**, *132*, 391–397. [[CrossRef](#)]
- Chen, X.P.; Huang, X.Y.; Zhang, Q.Y. Concentration-Dependent near-Infrared Quantum Cutting in  $NaYF_4: Pr^{3+}, Yb^{3+}$  phosphor. *J. Appl. Phys.* **2009**, *106*, 3–7. [[CrossRef](#)]
- Zhang, Q.Y.; Li, T.; Shi, D.M.; Yang, G.F.; Yang, Z.M.; Jiang, Z.H.; Buddhudu, S. Effects of  $PbF_2$  Doping on Structure and Spectroscopic Properties of  $Ga_2O_3-GeO_2-Bi_2O_3-PbO$  Glasses Doped with Rare Earths. *J. Appl. Phys.* **2006**, *99*, 2–5. [[CrossRef](#)]
- Zhang, Y.; Hu, S.; Tian, T.; Xiao, X.; Chen, Y.; Zhang, Y.; Xu, J. Growth and Spectral Properties of  $Er^{3+}$  and  $Yb^{3+}$  Co-Doped Bismuth Silicate Single Crystal. *Crystals* **2022**, *12*, 1532. [[CrossRef](#)]
- Xu, B.; Zhang, Y.P.; Yang, B.; Xia, H.P. Enhanced Cooperative Near-Infrared Quantum Cutting in  $Pr^{3+}-Yb^{3+}$  Co-Doped Phosphate Glass. *Optoelectron. Lett.* **2012**, *8*, 453–455. [[CrossRef](#)]
- Zhang, Q.Y.; Yang, C.H.; Pan, Y.X. Cooperative Quantum Cutting in One-Dimensional  $(YbxGd_{1-x})Al_3(BO_3)_4: Tb^{3+}$  Nanorods. *Appl. Phys. Lett.* **2007**, *90*, 4–7. [[CrossRef](#)]
- Adam, J. Lanthanides in Non-Oxide Glasses. *Chem. Rev.* **2002**, *102*, 2461–2476. [[CrossRef](#)]
- Yang, Z.; Feng, Z.; Jiang, Z. Upconversion Emission in Multi-Doped Glasses for Full Colour Display. *J. Phys. D. Appl. Phys.* **2005**, *38*, 1629–1632. [[CrossRef](#)]
- Zhang, Z.; Liang, Y. Synthesis and Upconversion Luminescence Properties of  $BaBiO_2Cl: Yb^{3+}, Er^{3+}$  Phosphor. *Crystals* **2022**, *12*, 1465. [[CrossRef](#)]
- Li, J.; Liu, J.; Yu, X. Synthesis and Luminescence Properties of  $Bi^{3+}$ -Doped  $YVO_4$  Phosphors. *J. Alloys Compd.* **2011**, *509*, 9897–9900. [[CrossRef](#)]
- Peng, M.; Wondraczek, L. Photoluminescence of  $Sr_2P_2O_7: Bi^{2+}$  as a Red Phosphor for Additive Light Generation. *Opt. Lett.* **2010**, *35*, 2544–2546. [[CrossRef](#)]
- Peng, M.; Da, N.; Krolkowski, S.; Stiegelschmitt, A.; Wondraczek, L. Luminescence from  $Bi^{2+}$ -Activated Alkali Earth Borophosphates for White LEDs. *Opt. Express* **2009**, *17*, 21169. [[CrossRef](#)]
- Razdobreev, I.; El Hamzaoui, H.; Ivanov, V.Y.; Kustov, E.F.; Capoen, B.; Bouazaoui, M. Optical Spectroscopy of Bismuth-Doped Pure Silica Fiber Preform. *Opt. Lett.* **2010**, *35*, 1341. [[CrossRef](#)]
- Ren, J.; Qiu, J.; Chen, D.; Hu, X.; Jiang, X.; Zhu, C. Luminescence Properties of Bismuth-Doped Lime Silicate Glasses. *J. Alloys Compd.* **2008**, *463*, 5–8. [[CrossRef](#)]

16. Meng, X.-G.; Meng, X.-G.; Qiu, J.-R.; Qiu, J.-R.; Peng, M.-Y.; Peng, M.-Y.; Chen, D.-P.; Chen, D.-P.; Zhao, Q.-Z.; Zhao, Q.-Z.; et al. Near Infrared Broadband Emission of Bismuth-Doped Aluminophosphate Glass. *Opt. Express* **2005**, *13*, 1628–1634. [[CrossRef](#)] [[PubMed](#)]
17. Kang, F.; Peng, M. A New Study on the Energy Transfer in the Color-Tunable Phosphor CaWO<sub>4</sub>:Bi. *Dalt. Trans.* **2014**, *43*, 277–284. [[CrossRef](#)] [[PubMed](#)]
18. Kravets, V.A.; Ivanova, E.V.; Orekhova, K.N.; Petrova, M.A.; Gusev, G.A.; Trofimov, A.N.; Zamoryanskaya, M.V. Synthesis and Luminescent Properties of Bismuth Borosilicate Glass Doped with Eu<sup>3+</sup>. *J. Lumin.* **2020**, *226*, 117419. [[CrossRef](#)]
19. Cao, J.; Wondraczek, L.; Wang, Y.; Wang, L.; Li, J.; Xu, S.; Peng, M. Ultrabroadband Near-Infrared Photoemission from Bismuth-Centers in Nitridated Oxide Glasses and Optical Fiber. *ACS Photonics* **2018**, *5*, 4393–4401. [[CrossRef](#)]
20. Tcibulnikova, A.V.; Myslitskaya, N.A.; Slezkin, V.A.; Bruykhannov, V.V.; Samusev, I.G.; Lyatun, I.I. Upconversion Luminescence Enhancement of the Ytterbium Oxide with Gold Nanoparticles on Anodized Titanium Surface. *J. Lumin.* **2022**, *251*, 119157. [[CrossRef](#)]
21. Lu, H.; Yang, J.; Huang, D.; Zou, Q.; Yang, M.; Zhang, X.; Wang, Y.; Zhu, H. Ultranarrow NIR Bandwidth and Temperature Sensing of YOF:Yb<sup>3+</sup>/Tm<sup>3+</sup> Phosphor in Low Temperature Range. *J. Lumin.* **2019**, *206*, 613–617. [[CrossRef](#)]
22. Zhuang, Y.; Wang, D.; Yang, Z. Upconversion Luminescence and Optical Thermometry Based on Non-Thermally-Coupled Levels of Ca<sub>9</sub>Y(PO<sub>4</sub>)<sub>7</sub>: Tm<sup>3+</sup>, Yb<sup>3+</sup> Phosphor. *Opt. Mater.* **2022**, *126*, 112167. [[CrossRef](#)]
23. Sharma, P.; Sharma, R.; Awana, V.P.S.; Narayanan, T.N.; Gupta, B.K.; Vashistha, N.; Tyagi, L.; Kumar, M. Low-Temperature Ultrafast Optical Probing of Topological Bismuth Selenide. *J. Alloys Compd.* **2021**, *886*, 161235. [[CrossRef](#)]
24. Artamonov, D.; Tcibulnikova, A.V.; Samusev, I.; Lyatun, I.; Bryukhanov, V. Spectral Shift of the Plasmon Maximum on the Rough Anodized Ti Surface in the Presence of PVA Films with Bi<sub>2</sub>O<sub>3</sub> and Bi<sub>2</sub>O<sub>3</sub>/Tm<sub>2</sub>O<sub>3</sub> Complexes. *Plasmonics* **2023**, *8*, 1232211. [[CrossRef](#)]
25. Tcibulnikova, A.V.; Slezkin, V.A.; Bruykhannov, V.V.; Samusev, I.G.; Kozhevnikov, A.S.; Savin, V.V.; Medvedskaya, P.N.; Lyatun, I.I. Cooperative Luminescence of Yb<sup>3+</sup> Ions of the Ytterbium Oxide Porous Surface. *Opt. Commun.* **2020**, *459*, 125006. [[CrossRef](#)]
26. Artamonov, D.A.; Tsibulnikova, A.V.; Slezkin, V.A. Reflection Dynamics of Tullium Oxide in Complex with Ytterbium and Bismuth Oxides in the Visible Wavelength Range. *KSTU News* **2023**, *68*, 127–134. [[CrossRef](#)]
27. De Bettencourt-Dias, A. *Luminescence of Lanthanide Ions in Coordination Compounds and Nanomaterials*; John Wiley & Sons Ltd.: Cardiff, UK, 2014; ISBN 9781118682760.
28. Tsuboi, T.; Murayama, H.; Shimamura, K. Low Temperature Luminescence of Tm<sup>3+</sup> Ions in LiYF<sub>4</sub> Crystal. *J. Alloys Compd.* **2006**, *408–412*, 776–779. [[CrossRef](#)]
29. Yuan, L.; Gu, S.; Zhang, X.; Zhao, Y.; Luo, W.; Wang, L.; Jiang, W. Low-Temperature Sintering of Bismuth-Doped Glass with High Fluorescence Properties from Mesoporous Silica SBA-15. *Ceram. Int.* **2020**, *46*, 1164–1170. [[CrossRef](#)]
30. Roy, A.; Dwivedi, A.; Kumar, D.; Mishra, H.; Rai, S.B. Enhanced Multimodal Behaviour of Tm<sup>3+</sup>/Yb<sup>3+</sup> Co-Doped YTaO<sub>4</sub> Ceramic Material through Bi<sup>3+</sup> Activation and Sensitization: Application as a Spectral Converter. *Ceram. Int.* **2020**, *46*, 24893–24905. [[CrossRef](#)]
31. Fan, B.; Liu, J.; Zhao, W.; Qi, S. Luminescence and Energy Transfer of a Single-Phased Phosphor Y<sub>2</sub>GeO<sub>5</sub>: Bi<sup>3+</sup>, Tm<sup>3+</sup>, Tb<sup>3+</sup>, Eu<sup>3+</sup> for White UV LEDs. *Opt. Mater.* **2019**, *90*, 33–39. [[CrossRef](#)]
32. Auzel, F. Upconversion and Anti-Stokes Processes with f and d Ions in Solids. *Chem. Rev.* **2004**, *104*, 139–174. [[CrossRef](#)] [[PubMed](#)]
33. Tian, X.; Weidong, Z.; Xiangzhong, C.; Chunlei, Z.; Xiaoming, T.; Xiaowei, H. Low Temperature Luminescence Properties of Tm<sup>3+</sup> Doped Aluminate Phosphor. *J. Rare Earths* **2006**, *24*, 141–144. [[CrossRef](#)]

**Disclaimer/Publisher’s Note:** The statements, opinions and data contained in all publications are solely those of the individual author(s) and contributor(s) and not of MDPI and/or the editor(s). MDPI and/or the editor(s) disclaim responsibility for any injury to people or property resulting from any ideas, methods, instructions or products referred to in the content.